Graphene supercapacitor with both high power and energy density

Article *in* Nanotechnology · August 2017

DOI: 10.1088/1361-6528/aa8948

6 authors, including:

Hao Yang
The Ohio State University
8 PUBLICATIONS **23** CITATIONS
SEE PROFILE

Jae-Hyung Jang
Gwangju Institute of Science and Technology
108 PUBLICATIONS **652** CITATIONS
SEE PROFILE

Wu Lu
The Ohio State University
129 PUBLICATIONS **1,889** CITATIONS
SEE PROFILE

PAPER

Graphene supercapacitor with both high power and energy density

IOP Publishing Nanotechnology
Nanotechnology 28 (2017) 445401 (10pp) https://doi.org/10.1088/1361-6528/aa8948

Graphene supercapacitor with both high power and energy density

Hao Yang[1], Santhakumar Kannappan[2], Amaresh S Pandian[3], Jae-Hyung Jang[2], Yun Sung Lee[3] and Wu Lu[1,2]

[1] Department of Electrical and Computer Engineering, The Ohio State University, Columbus, Ohio 43210, United States of America
[2] Department of Nanobio Materials and Electronics, Gwangju Institute of Science and Technology, Gwangju 500-712, Republic of Korea
[3] Faculty of Applied Chemical Engineering, Chonnam National University, Gwangju 500-757, Republic of Korea

E-mail: lu.173@osu.edu

Received 16 July 2017, revised 22 August 2017
Accepted for publication 30 August 2017
Published 4 October 2017

Abstract

Supercapacitors, based on fast ion transportation, are specialized to provide high power, long stability, and efficient energy storage using highly porous electrode materials. However, their low energy density excludes them from many potential applications that require both high energy density and high power density performances. Using a scalable nanoporous graphene synthesis method involving an annealing process in hydrogen, here we show supercapacitors with highly porous graphene electrodes capable of achieving not only a high power density of 41 kW kg^{-1} and a Coulombic efficiency of 97.5%, but also a high energy density of 148.75 Wh kg^{-1}. A high specific gravimetric and volumetric capacitance (306.03 F g^{-1} and 64.27 F cm^{-3}) are demonstrated. The devices can retain almost 100% capacitance after 7000 charging/discharging cycles at a current density of 8 A g^{-1}. The superior performance of supercapacitors is attributed to their ideal pore size, pore uniformity, and good ion accessibility of the synthesized graphene.

Supplementary material for this article is available online

Keywords: graphene, supercapacitor, energy storage, nanoporous material

(Some figures may appear in colour only in the online journal)

1. Introduction

Supercapacitors have drawn great attention because of their high charge–discharge rate, long cycle life, outstanding power density, and no short circuit issue that has been always a concern for current batteries and fuel cells [1–3]. Also known as ultracapacitors or electrochemical capacitors, supercapacitors store energy with electric double-layer (EDL) capacitance (ion adsorption) or pseudocapacitance (surface redox reaction). Although pseudocapacitors using conducting polymers or metal oxides as electrode materials can have a high faradaic capacitive performance, they cannot maintain it after long cycling. On the other hand, EDL capacitors with porous carbon electrodes can be charged and discharged as many as one million cycles without performance degradation [4]. Furthermore, the ion transportation in EDL capacitors is faster than the redox reaction in pseudocapacitors, leading to a high charge–discharge rate and power density in EDL capacitors. Currently the major drawback of EDL capacitors is the low energy density, generally in the range of 3–5 Wh kg^{-1} [5, 6], which is one to two orders of magnitude lower than commercialized lithium-ion batteries [6]. Supercapacitors with increased energy storage but little sacrifice of power density are critically needed for practical applications, such as plug-in hybrid electric vehicles [7], wind turbine energy storage [8], regenerative braking [9], and uninterrupted power supply [10].

To improve the energy density, a porous electrode material with a high surface area and low equivalent series resistance (ESR) is desired. Carbon materials, due to their low cost, microtexture and processing latitude, are more attractive than other electrode materials. Activated carbons, carbon aerogels, and carbon nanotubes have been widely exploited [6]. Activated carbons are common materials in commercial EDL supercapacitors. The reported specific surface area of activated carbon ranges from 500 to 2000 $m^2 g^{-1}$ [11, 12], only a fraction of which can contribute to energy storage. This is because the activated carbon materials have poor uniformity in pore sizes ranging from micropores (~0.3 nm) to macropores [13]. In such materials, the micropores are inaccessible to electrolyte solutions [14] and macropores result in a low surface volume ratio, both of which lead to a low specific capacitance [15]. Carbon nanotubes have a moderate surface area and good conductivity. However, supercapacitors based on carbon nanotubes do not exhibit good capacitive performance [16]; manufacturing difficulties and cost limit their applications in energy storage devices.

A more promising electrode candidate to overcome the low capacitance for the EDL supercapacitors is graphene. Graphene, due to its unique lattice structure, has many appealing properties, like electrical conductivity, chemical stability, and mechanical stiffness. A monolayer of sp^2 bonded carbon atoms can reach a surface area of 2675 $m^2 g^{-1}$ [17, 18], basically setting the upper limit for all carbon materials. With improvements in the exfoliation and reduction techniques of graphite oxide (GO), graphene-based materials can be produced in largescale at a very low cost. A variety of oxidation-exfoliation methods have been employed to minimize the agglomeration between the graphene sheets, such as chemical reduction [14, 19], microwave irradiation [20], thermal annealing [21, 22], and powerful sonication [23]. Chemical reduction methods generally involve harmful reducing agents and are not suitable for mass production [19]. Thermal annealing can produce high quality graphene sheets, but at a very high temperature (~1050 °C) [21]. The irradiation and sonication methods serve as pure exfoliation techniques and always require the help of chemical reduction [20, 23]. The reported graphene-based supercapacitors have achieved 85.6 Wh kg^{-1} (154 F g^{-1}) under hydrazine reduction [14], 70 Wh kg^{-1} (166 F g^{-1}) with microwave exfoliation [24], and 1.36 mWh cm^{-3} (276 F g^{-1}) by laser scribing [25]. Though tremendous progress has been made, state-of-the-art supercapacitors still suffer from lower energy density than lithium ion batteries [6]. In our earlier work, we demonstrated a specific capacitance of 284 F g^{-1} in supercapacitors with graphene electrodes annealed in vacuum at 150 °C [26]. Here we show synthesized mesoporous graphene materials by a one-step hydrogen annealing with a pore size of a few nanometers and uniform pore size distribution. Supercapacitors made of these graphene electrodes have a specific capacitance of 306 F g^{-1} and an energy density of 148.75 Wh kg^{-1}, capable of achieving simultaneously a high power density and energy density. $EMIMBF_4$ and $LiPF_6$ electrolytes are used to achieve a high energy storage capability due to their higher potential windows than aqueous electrolytes. They have also a wider temperature tolerance than aqueous electrolytes.

2. Results and discussion

The synthesis process is based on the exfoliation and reduction reaction of GO with the assistance of hydrogen gas at a relatively low temperature (figure 1(a)). The GO is heavily oxygenated with a basal plane mainly occupied by epoxide (O–C–O), carbonyl (C=O), hydroxyl (C–OH) and carboxyl (COOH) groups [27, 28]. With the presence of heat, oxygen containing groups are reduced by hydrogen to form water vapor and CO_2 between GO layers. When evolved gases accumulate, a high pressure is generated to break the agglomeration, where the reduced GO is converted into hydrogen annealed graphene (HAG). The process can be visually observed with the color change from brown to black (related to reduction) and large volume expansion (related to exfoliation).

The FESEM images (figure 1(b)) show the typical porous structure of HAG surface. They reveal the successful exfoliation under which a large area of restacking layers has been peeled off so that it shows obvious gaps between them. The TEM images (figures 1(c), (d)) show the morphology of HAG, where the agglomeration is very limited. From TEM images, there is either a monolayer or few layers of graphene at the edges of HAG sheets. Away from edges, the wrinkle nature of HAG sheets is clearly observed, providing more adsorption sites for ionic charges. As shown in figure 1(d), the average widths of the two wrinkles are 4.12 nm and 0.94 nm, which fall in the mesoporous and microporous range, respectively.

To characterize the porosity, the nitrogen isothermal adsorption experiment was performed at liquid nitrogen temperature. The result shows a type IV adsorption isothermal curve with a hysteresis loop (figure 2(a)) [29]. The hysteresis loop between adsorption and desorption along with a sharp fall at a relatively high pressure suggests the slit geometry of major mesopores [30], which appears to be in good agreement with the electron microscopy images (figures 1(b)–(d)). The HAG demonstrates a Brunauer–Emmett–Teller (BET) specific surface area of 410 $m^2 g^{-1}$, which is extracted from the linear region of $1/[V_a(p_0/p - 1)]$ versus p/p_0 in the classical BET range of 0.05–0.3 (inset of figure 2(a)) [31]. The BET surface area is not necessarily indicative of the functional area for electrolyte ions. The classic Gouy–Chapman–Stern model fails to predict the performance parameter in systems with high ion concentration or systems with ion size comparable to the average pore size [32]. Indeed, the charge storage is affected by multiple factors, such as the complex pore shape, interaction between carbon atoms, solvent molecules and ions, and the electrosorption-induced electrode swelling [32–34]. Therefore, the device performance cannot be simply evaluated by the BET surface area. The energy storage performance can only be characterized by electrochemical measurements on assembled supercapacitor cells.

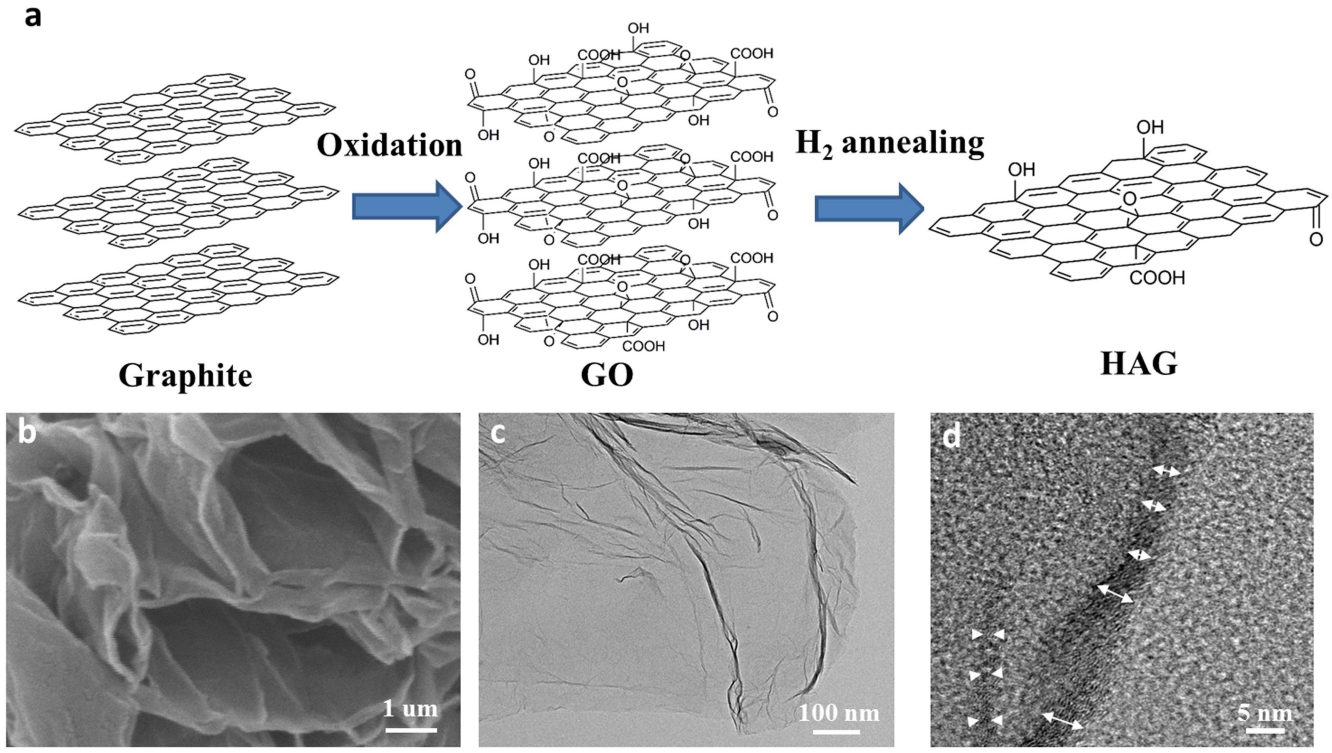

Figure 1. (a) Schematic demonstrating the process of one step exfoliation and reduction process of GO with low temperature hydrogen annealing. During this process, hydrogen gas reacts with oxygen related groups forming water vapor resulting in the exfoliation of the restacked layers. (b) A FE-SEM image of the HAG piece. (c) A TEM image of a HAG sheet. It reveals the typical morphology of those graphene materials. (d) A higher resolution TEM image of wrinkled structures in HAG. It is found that the average widths of the two wrinkles are around 4.12 nm and 0.94 nm, respectively.

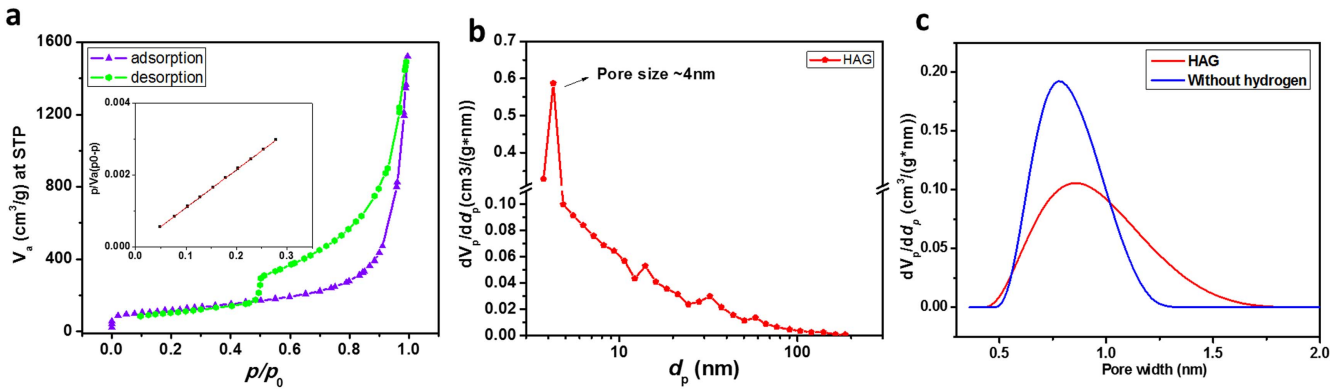

Figure 2. (a) Nitrogen adsorption/desorption plot at 77.4 K of the HAG sample. Inset gives the plot of $1/[V_a(p_0/p-1)]$ versus p/p_0 in the classical BET range of 0.05–0.3, based on which the specific surface area is extracted. The type IV adsorption isothermal curve with a hysteresis loop suggests the near cylindrical or slit geometry of major pores. (b) Pore-size distribution of the HAG sample. The pore volume of mesopores (2–50 nm) in HAG is 77.7% of the total pore volume. (c) Microporous pores size distribution in HAG and samples annealed without hydrogen. To derive a meaningful micropore size distribution, the nitrogen adsorption isotherm is analyzed with a heterogeneous slit NLDFT model using SAIEUS software package [37, 38]. The stable output is calculated with a regulation method in conjugation with a L-curve method to minimize the fluctuation of the results [39, 40].

The pore size distribution of the synthesized material was characterized by the classical Barret–Joyner–Halenda (BJH) method (figure 2(b)) and modern non-local density function theory (NLDFT) (figure 2(c)). The BJH is the standard procedure for calculating the pore size in the mesoporous materials. The BJH method is based on the modified Kelvin equation, in which the radius of the capillary in the Kelvin equation is replaced by the pore radius subtracting the adsorbed film thickness. Based on the intermolecular potentials of fluid–fluid and fluid–solid interactions, the molecular models such as NLDFT and Monte Carlo simulations provide a more accurate description of the adsorption, especially in the smaller pore size range. Two peaks at 4.27 and 0.86 nm were observed (figures 2(b), (c)), comparable to the wrinkle widths shown in figure 1(d). The high peak sharpness in figure 2(d) suggests the good uniformity of mesopores. The

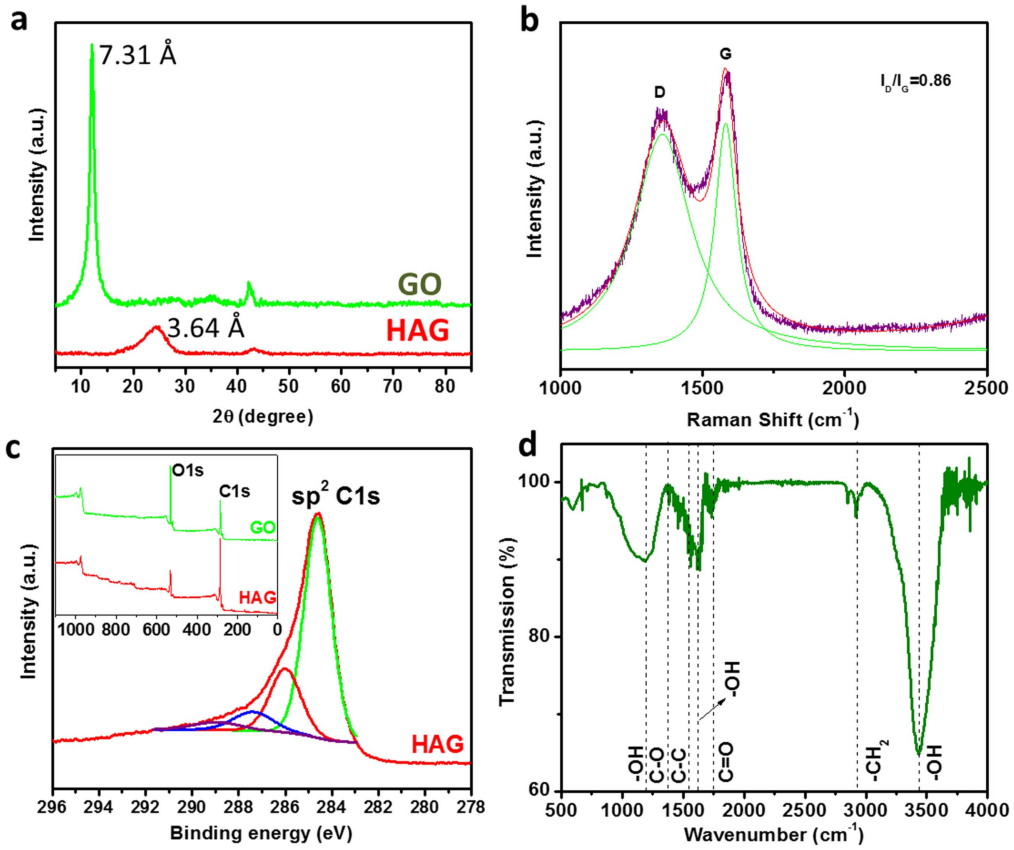

Figure 3. (a) XRD spectra of GO and HAG samples showing the interlayer spacing decrease after the exfoliation and reduction. (b) Raman spectrum of the HAG sample with Lorentzian fittings. (c) XPS C1s spectrum of the HAG sample and the inset is the comparison between GO and HAG. (d) FTIR spectrum of the HAG powder.

pore volume for the pores at 0.86 nm is 0.11 cm^3 $(g^*nm)^{-1}$, while the pore volume at the 4.27 nm is 0.59 cm^3 $(g^*nm)^{-1}$. Compared with another sample annealed at the similar temperature range without hydrogen (in vacuum) [26], the HAG has more uniform pore size distribution and reveals less micropores (figure 2(c)). Theoretical and experimental investigations on hydrogen absorption on carbon-based materials [35, 36] have suggested that hydrogen prefers to adsorb on pores in microporous range. Our hypothesis is that the oxide groups in the micropores react with the hydrogen generating gases. The evolved gases expand the pores into the mesoporous size range. This explains why hydrogen reduction can generate more uniform mesopores range than micropores.

There has been theoretical work reported to study the dependence of specific capacitance on pore sizes by Monte Carlo, molecular dynamics, densify function theory simulations [41–44]. In microporous range, the specific capacitance is found to increase greatly when the average pore size of carbon electrodes approaches the diameter of electrolyte ions [41–43]. However, it is essentially impossible to have a very precise control of pore size that falls exactly at the electrolyte ions size. A slightly smaller or larger pore size would cause the capacitance to decrease significantly. In the mesoporous range, it is found that the capacitance oscillates with the pore size and becomes stabilized when approaching eight times the ion diameter [44]. The diameters of the $EMIM^+$ and BF_4^- are approximately 0.54 and 0.31 nm, respectively, eightfold values are 4.32 and 2.48 nm. The pore size of HAG falls in this range and a high specific capacitance would be expected.

The interlayer spacing of graphite is approximately 3.35 Å [45]. The XRD features of GO show an intense (002) peak occurring at 12.06° with a d-spacing of 7.31 Å, due to the oxide groups between the basal planes after oxidation. Upon hydrogen treatment, the GO diffraction peak disappears and a new peak with reduced intensity and broadened width appears around 24.44° for HAG (figure 3(a)). The interlayer spacing of the reduced product decreases to a much smaller value of 3.64 Å, which suggests the removal of oxygen containing groups by reaction with hydrogen molecules under heat. Due to the residual oxide groups distributed randomly, the interlayer spacing is not as uniform as graphite leading to a broadened and weak (002) peak.

The Raman spectrum of highly-ordered graphite shows an intense G band around 1580 cm^{-1} resulting from the in-phase vibration of graphite lattice, as well as a weak D band around 1355 cm^{-1} caused by slight disorders [46]. Because of the amorphization happening in the oxidation, the GO contains some sp^3 bonded carbons [47]. Therefore, a broad and relatively intense D band is observed [48]. The oxidation of GO generates some defects [21, 48], such as the 5-8-5 defects [49] and Stone–Wales defects (5-7-7-5 rings) [50]. After Lorentzian fitting of Raman spectrum of HAG (figure 3(b)),

the D-band caused by disordered structure can be found approximately at 1350.96 cm^{-1}, and the G-band corresponding to E_{2g} mode at the center of Brillouin zone locates at ~1582.85 cm^{-1} [51]. The intensity ratio of HAG D-band and G-band, I_D/I_G, is about 0.86 less than 1.0, indicating the restoring of the π-conjugated structure [51]. Compared with the GO (figure S1(a) is available online at stacks.iop.org/NANO/28/445401/mmedia), the I_D/I_G ratio of HAG decreases slightly, which is caused by the removal of weak carbon–carbon bonds during hydrogen annealing.

In XPS (figure 3(c)), from GO to HAG the C/O ratio increases from 2.02 to 5.11 with O1s peak reduced significantly. By performing Gaussian–Lorentzian fitting, the intense C–C peak is observed at a binding energy of 284.6 eV showing the sp^2 bonding. The broad tail towards higher binding energy up to 296 eV is because of the contributions of various carbon bonding configurations. Those multiple peaks at 285.99, 287.37, 288.93 eV are typically assigned to oxygen containing groups C–OH (or C–O–C), C=O, and COOH, respectively [52]. The existence of C–O–C, which is widely seen in the graphene oxide system, has a similar C1s binding energy to C–OH [53]. Compared with GO (figure S1(b)), the C–OH peak is much lower in HAG indicating the successful reduction. Another confirmation of the reduction is obtained by the FTIR shown in figure 3(d). In HAG, the broad and intense peak at 3433 and 1637 cm^{-1} correspond to the OH stretching in water molecules, indicating that there are lots of H_2O generated after reduction [30]. This phenomenon is consistent with our hypothesis of hydrogen reduction with water vapor as the reaction product. Moreover, the C=C stretching is observed at 1560 cm^{-1}. Other than the two peaks, the peaks at 1719 cm^{-1}, 1383 cm^{-1}, and 1190 cm^{-1} are related to the C=O, C–O, and –OH stretching in COOH, respectively [54]. The weak intensities of these peaks suggest an efficient removal of those functional groups. The asymmetric and symmetric stretching peaks of $–CH_2$ at 2918 and 2851 cm^{-1} reveal the restoration of carbon basal planes owing to hydrogen reduction [32, 55].

To evaluate the electrochemical performance of HAG electrodes, supercapacitors were assembled in a symmetrical cell geometry using ionic liquid $EMIMBF_4$ and $LiPF_6$ as electrolytes. An ideal capacitor should retain a constant current during the cyclic voltammetry (CV) scans after being fully charged or discharged because of the relation $I(t) = C(dV/dt)$ [56]. The CV curves of HAG electrodes in $EMIMBF_4$ and $LiPF_6$ measured from 5 to 100 mV s^{-1} indicate a good capacitive behavior (figures 4(a), (b)). The ionic liquid $EMIMBF_4$ has moderate conductivity and can work under a high voltage up to 4.3 V [14, 57], which brings significant benefits in improvement of energy density. The galvanostatic charge–discharge measurements were taken at various current densities (figures 4(c), (d) and S2). The linear discharging curves illustrate a close-to-ideal EDL capacitor performance. The voltage drop at the beginning of discharging is due to the voltage loss across the ESR.

The Nyquist plots and the fitting curves of the HAG supercapacitors are shown in figure 5. The Nyquist plot of the HAG supercapacitors contains a straight line in low frequency region related to the capacitive element, and an arc in the high frequency region related to the resistances. The internal resistance is 4.26 Ω for $EMIMBF_4$ from the x-intercept of the high-frequency arc, leading to a high charge/discharge rate and high power density. The Warburg impedance is the result of frequency dependence of ion diffusion in the electrolyte to the electrode interface. It appears in the Nyquist plot as a diagonal line with a slope around 45° between the semicircle and spike. By fitting the electrochemical impedance spectroscopy (EIS) data, it is found that the Warburg impedance of our HAG electrode is as small as 4.0 Ω and the Warburg characteristic frequency is as high as 9.9 rad s^{-1}, suggesting a short diffusion path in HAG [58]. Short diffusion path and fast migration of the electrolyte ions to the nanopores in HAG electrode result in an efficient utilization of the porous structure of HAG electrodes [59]. For our HAG sample, the impedance curve shows a near vertical line in the low frequency region which suggests that the HAG supercapacitor behaves close to an ideal capacitor.

The following equation explains how we extract the specific gravimetric capacitance from galvanostatic charge–discharge curves [20, 24, 60].

$$C_s = \frac{4C}{m} = \frac{4I\Delta t}{m\Delta V}, \tag{1}$$

where C is the capacitance of the cell, I is the constant current, Δt is the discharging time (except the voltage drop), m is the total weight of electrode materials, and ΔV is the voltage drop during discharging process (except the voltage drop on ESR). The reported specific capacitance of graphene supercapacitors in ionic liquid is in the range of 100–250 F g^{-1} at a current density of 1 A g^{-1} [14]. At 1 A g^{-1}, the sample annealed without hydrogen (in vacuum) in our earlier study has a specific capacitance of 284 F g^{-1} [26]. The experimental specific capacitance values of the HAG electrode in ionic liquid are 306.03, 256.19, 239.47, 216.99, 180.30 and 146.77 F g^{-1} at current densities of 1, 2, 2.5, 4, 5 and 8 A g^{-1}, respectively (figure 6(a)). The specific capacitance values in $LiPF_6$ are 111.10, 95.33 and 90.09 F g^{-1} at 1, 2.5 and 4 A g^{-1}, respectively (figure 6(a)). Note that these values are based on the total weight of single electrode materials including graphene and additives. The values of volumetric capacitance are 64.27 F cm^{-3} and 23.33 F cm^{-3} at 1 A g^{-1} in $EMIMBF_4$ and $LiPF_6$, respectively, in comparison with the state of the art values (table 1). The lower specific capacitances of $LiPF_6$ at the same current densities are due to the lower ion concentration and breakdown voltage. Because the pore size of HAG is few times larger than the size of electrolyte ions, ions can easily accommodate inside the HAG electrodes leading to better electrolyte accessibility and utilization of the surface within the pores.

The energy densities at different current densities were obtained using the following formula [24, 25, 60]:

$$E = \frac{1}{2}CV^2 = \frac{1}{8}C_sV^2. \tag{2}$$

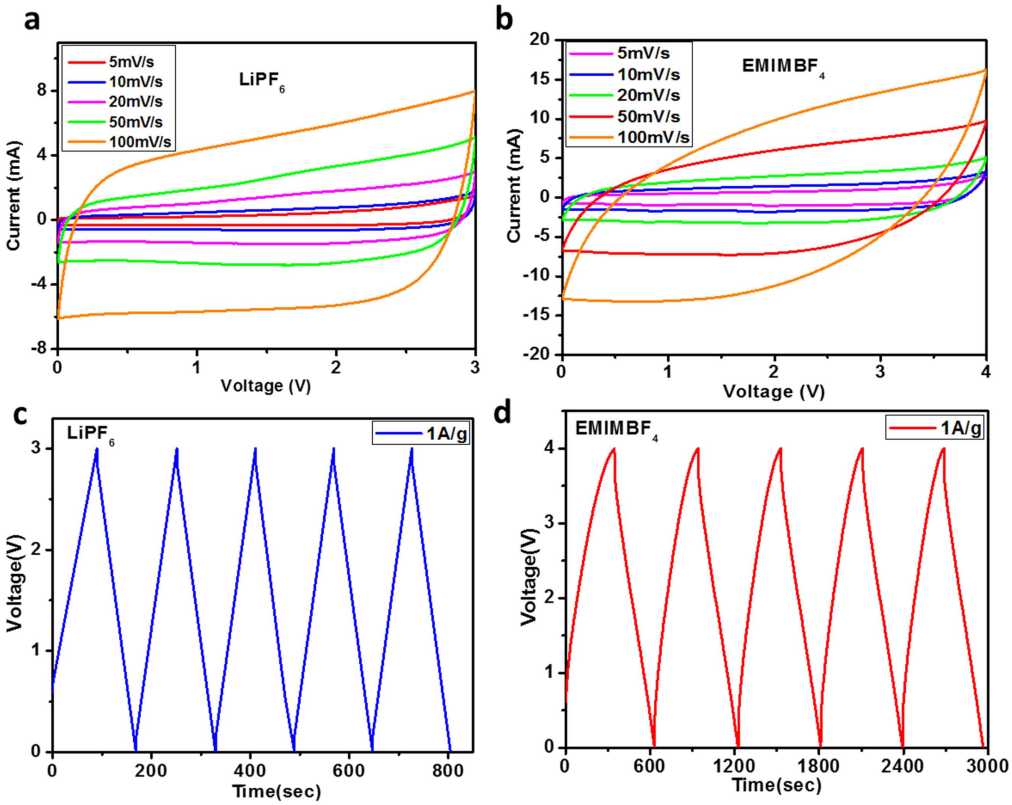

Figure 4. CV curves of HAG electrode in (a) $LiPF_6$ and (b) $EMIMBF_4$ at different scan rates. Galvanostatic charge–discharge curves of supercapacitor in (c) $LiPF_6$ and (d) $EMIMBF_4$ for different current densities.

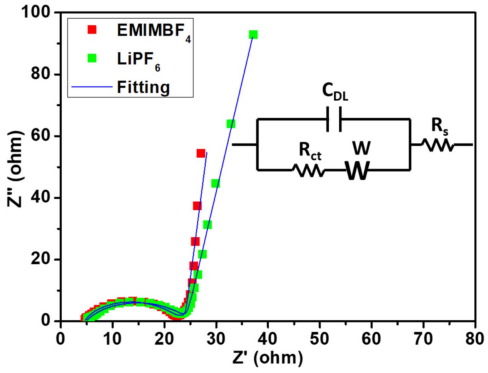

Figure 5. Nyquist plot from EIS measurement and the fitting curves. The inset shows the equivalent circuit of a supercapacitor containing double layer capacitor C_{DL}, charge transfer resistance R_{ct}, series resistance R_s and Warburg element W.

The corresponding power density was calculated according to:

$$P = \frac{E}{\Delta t}. \tag{3}$$

The maximum power density at the matched impedance condition was evaluated with [6, 24, 25, 50]

$$P = \frac{V^2}{4mR_{ESR}}, \tag{4}$$

where R_{ESR} is the ESR value calculated by $R_{ESR} = V_{ESR}/2I$. To reveal the energy storage performance, the Ragone plots of supercapacitors in $EMIMBF_4$ and $LiPF_6$ are shown in figure 6(b). An ultra-high gravimetric energy density of 148.75 Wh kg^{-1} (in $EMIMBF_4$, volumetric value 31.24 mWh cm^{-3}) at 1 A g^{-1} was achieved with ionic liquid at room temperature. The HAG electrodes in $LiPF_6$ have an energy density 31.39 Wh kg^{-1} due to the smaller potential window [57]. There are several reasons that $EMIMBF_4$ electrolyte performs better than $LiPF_6$: 1. the potential window of $EMIMBF_4$ is wider than $LiPF_6$ leading to higher energy stored. 2. The solvated Li ions are surrounded by solvent molecules, leading to a larger solvated cation size [61, 62]. With a larger cation size, it was found that the diffusion coefficient decreases [63]. By fitting the EIS data, it is found that the Warburg impedance of $LiPF_6$ is larger than that of the $EMIMBF_4$, suggesting a smaller diffusion coefficient in $LiPF_6$ [58]. A smaller diffusion coefficient leads to an increased ionic resistance and reduced capacitance as the ions cannot efficiently move through electrolytes [63, 64]. 3. $EMIMBF_4$ is only composed with bulk cations and anions, resulting in a higher ion concentration and capacitance. 4. Some other advantages of $EMIMBF_4$ over $LiPF_6$ are high thermal and electrochemical stability, non-flammability, non-combustibility and lack of reactivity in electrochemical applications [65]. However, the devices with $LiPF_6$ demonstrated a higher power density of 47 kW kg^{-1} at the matched impedance condition compared with 41 kW kg^{-1} for devices with $EMIMBF_4$ due to the slightly smaller ESR in $LiPF_6$ as shown in figure 4. The previous reported gravimetric energy density values of graphene supercapacitors are among 20–90 Wh kg^{-1} at 1 A g^{-1} [14, 24, 25, 66], and the volumetric

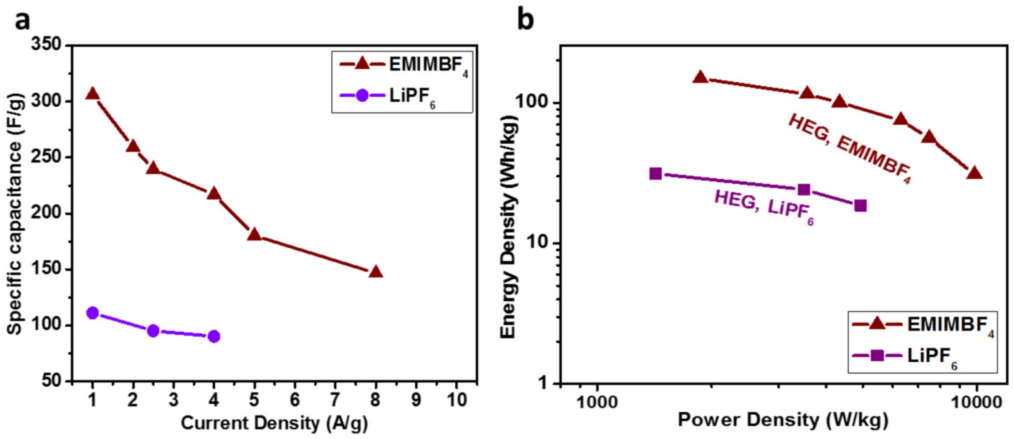

Figure 6. (a) Specific capacitance versus current density for HAG supercapacitors. (b) Comparative Ragone plots of the developed HAG supercapacitors in $EMIMBF_4$ and $LiPF_6$.

Table 1. Performance comparison of reported graphene-based supercapacitors. The table shows the comparison of electrochemical performance of reported state-of-the-art graphene supercapacitors with the HAG supercapacitors in this work. The conversion from gravimetric to volumetric values is calculated based on package density $\rho = m/V_e = 0.21$ g cm^{-3}, where V_e is the volume of the electrode and m is the mass of the material loaded.

Material	Electrolyte	Current density (A g^{-1})	Specific capacitance (F g^{-1}/F cm^{-3})	Energy density (Wh kg^{-1}/ mWh cm^{-3})	Power density (kW kg^{-1}/ kW L^{-1})
Curved graphene [14]	$EMIMBF_4$	1	154.1/46.2	85.6/25.68	1.14/0.34
a-MEGO [24]	Organic electrolyte	1	166/60	~70/23	N/A
LSG [25]	Organic electrolyte	~1	276/13.2	28.33/1.36	N/A
EM-CCG film [66]	Organic electrolyte	1	167.1/208.9	88.24/110.3	6.88/8.6
HAG (This work)	$EMIMBF_4$	1	306.03/64.27 F	148.75/31.24	30.95/6.50
	$LiPF_6$	1	111.10/23.33	31.39/6.59	30.65/6.44

energy density values are in the range of 1.36–25.68 mWh cm^{-3} for supercapacitors with no special compression methods applied [14, 24, 25]. Compared with reported graphene supercapacitors, our HAG supercapacitors have both higher gravimetric and volumetric energy density and specific capacitance at the same current density of 1 A g^{-1} (table 1). Assuming that 30% weight of a packaged supercapacitor cell is contributed by the electrode materials, the calculated systematical energy density for our device would be approximately 45 Wh kg^{-1}, which is one order higher than the commercial supercapacitors that use activated carbon as the electrode material [8]. As discussed above, such excellent electrochemical performance is attributed to close-to-ideal pore size for maximum ion access ability and the uniform pore size.

For supercapacitors, the energy is stored in electrochemical form and gets released as electric energy. During the conversion, the energy loss of supercapacitors is dependent on joule heating, charge redistribution, leakage loss, decomposition, and the initial state of devices. The energy conversion efficiencies of energy storage devices reflect the capability to convert the energy from one form into another. The columbic efficiency is defined as the total charge removed divided by the total charge added to compensate the charge removed, shown in equation (5). The resulted Coulombic efficiency is 97.5%, calculated from figure 4(c). The round-trip efficiency is the ratio of total input energy and released energy during the charging and discharging process, shown in equation (6). The round-trip efficiency of our devices is as high as 88.9%, which is comparable with Li-ion batteries (80%–90%).

$$\eta_{\text{Coulombic}} = \frac{\text{Total charge released}}{\text{Total charge stored}} = \frac{\text{Discharing time}}{\text{Charging time}} \quad (5)$$

$$\eta_{\text{Round-trip}} = \frac{\text{Total released energy}}{\text{Total input energy}} = \frac{\text{Area under the discharging curve}}{\text{Area under the charging curve}} \quad (6)$$

The stability of HAG electrodes is confirmed by long cycling tests. The HAG supercapacitor was charged and discharged for 10 000 cycles (figure 7). The first 3000 cycles were performed at two low current densities (4 and 5 A g^{-1}) to predetermine the cycle numbers, and the next 7000 cycles were performed at high current density (8 A g^{-1}) to examine the cycling stability. Almost 100% of the initial specific capacitance was retained in ionic liquid at the high current density.

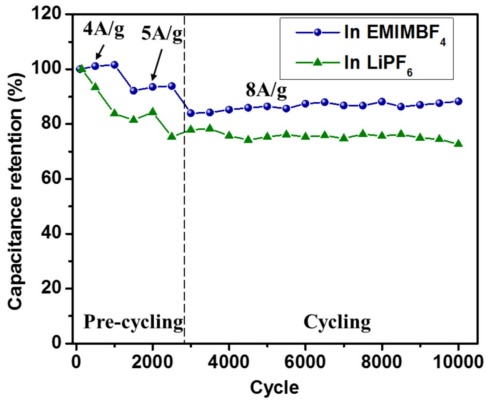

Figure 7. The specific capacitance retention of HAG supercapacitors in $EMIMBF_4$ and $LiPF_6$ as a function of cycling times.

3. Experiments

3.1. Preparation of GO

GO was synthesized following modified Hummer's method, which has been described in our earlier work [26]. Briefly, graphite powder was mixed with concentrated sulfuric acid, potassium persulfate and phosphorus pentoxide for pre-oxidation. The preliminarily oxidized graphite was mixed with sulfuric acid in an ice bath. Potassium permanganate was added gradually with continuous stirring and cooling to keep the temperature below 35 °C. Distilled water and H_2O_2 were added to stop the reaction. To remove metal ions, the solution was washed with hydrochloric acid and dialyzed for two weeks.

3.2. Preparation of HAG

After vacuum-drying, GO powder was put into a quartz furnace under flowing argon and heated at 200 °C. When reaching the temperature, argon was evacuated followed by introducing hydrogen gas at a pressure of 110 T for 3 min. With the presence of heat, the oxygen containing group is reduced by hydrogen to form water vapor between the GO layers. When water vapor accumulates, a high pressure is generated to break the attractive forces, where the reduced GO is converted into HAG.

3.3. Electrode preparation and cell assembly

The electrode preparation and cell assembly process is the same as described in [26]. The diameter of each electrode is around 0.8 cm and the thickness is 0.1 mm. Each electrode weighs about 1 mg. The estimated inter-sheet spacing is 3.67 nm (support information section 2). This process enhances the integration of the electrolytes with the nanoporous graphene electrode materials to form a compact ion transport network.

Two HAG electrodes were assembled in symmetrical cell geometry in CR2032 cell cases in glove box. The separator used is porous polypropylene film. The electrolytes are pure ionic liquid 1-ethyl-3-methylimidazolium tetrafluoroborate ($EMIMBF_4$) and 1.0 M $LiPF_6$ in ethylene carbonate/diethyl carbonate solution.

3.4. Electrochemical measurement

The CV was accomplished with CH Instruments CHI760D. Charging and discharging characteristics were tested with NAGANO BTS-2004H battery tester. The EIS measurement was analyzed with Zahner Electrochemical Unit 1M6e.

4. Conclusions

In summary, the single-step annealing process obviates the use of toxic reducing reagents and time-consuming process, and enables high quality graphene materials with uniform pore size for high performance EDL supercapacitors. The material characterizations of the synthesized graphene reveal that the HAG sheets have a mesoporous surface and reduced oxide groups for charge storage in EDL capacitors. The systematic study of the electrochemical performance of HAG electrodes shows excellent energy storage performance owing to the wrinkled and porous morphology of the material. High energy density (148.75 Wh kg^{-1}) and high power density (41 kW kg^{-1}) were simultaneously achieved in the devices with ionic liquid electrolyte. The cycling stability study shows very stable specific capacitance at 8 A g^{-1} current density.

Utilizing the excellent charge storage capability of graphene requires that the material can be processed with an efficient, industry-compatible and low cost way that is ready to scale for mass production. The approach in this work shows a viable supercapacitor technology with both high power density and energy density. The superior electrochemical performance of the HAG supercapacitors meets the power, energy, and durability requirements [7]. The appealing properties of this graphene supercapacitor technology could bring in new electrochemical energy storage applications with both high power and energy requirements.

Acknowledgments

This work is partially supported by the World Class University program by the National Research Foundation of Korea (Project No. R31-10026) and National Science Foundation.

Author contributions

WL conceived the experiments. HY and SK synthesized the material. HY performed the analysis and calculation based on the discussion with WL and SK. ASP prepared the electrode and assembled the supercapacitor cell. YSL, and JHJ provided instrumentation support. HY wrote the manuscript. WL and HY revised and finalized the manuscript.

ORCID iDs

Hao Yang https://orcid.org/0000-0003-1056-9447
Amaresh S Pandian https://orcid.org/0000-0002-9203-6865
Wu Lu https://orcid.org/0000-0001-6776-9082

References

[1] Armand M and Tarascon J M 2008 Building better batteries *Nature* **451** 652–7

[2] Wu H *et al* 2013 Stable Li-ion battery anodes by *in situ* polymerization of conducting hydrogel to conformally coat silicon nanoparticles *Nat. Commun.* **4** 1943

[3] Park C M *et al* 2010 Li-alloy based anode materials for Li secondary batteries *Chem. Soc. Rev.* **39** 3115–41

[4] Miller J R and Simon P 2008 Electrochemical capacitors for energy management *Science* **321** 651–2

[5] Simon P and Gogotsi Y 2008 Materials for electrochemical capacitors *Nat. Mater.* **7** 845–54

[6] Burke A 2000 Ultracapacitors: why, how, and where is the technology *J. Power Sources* **91** 37–50

[7] Burke A 2007 Batteries and ultracapacitors for electric, hybrid, and fuel cell vehicles *Proc. IEEE* **95** 806–20

[8] Abbey C and Joos G 2007 Supercapacitor energy storage for wind energy applications *IEEE Trans. Ind. Appl.* **43** 769–76

[9] Dixon J W and Ortuzar M E 2002 Ultracapacitors+DC–DC converters in regenerative braking system *IEEE Aerosp. Electron. Syst. Mag.* **17** 16–21

[10] Lahyani A, Venet P, Guermazi A and Troudi A 2013 Battery/supercapacitors combination in uninterruptible power supply (UPS) *IEEE Trans. Power Electron.* **28** 1509–22

[11] Qu D 2002 Studies of the activated carbons used in double-layer supercapacitors *J. Power Sources* **109** 403–11

[12] Fernandez J A *et al* 2008 Performance of mesoporous carbons derived from poly(vinyl alcohol) in electrochemical capacitors *J. Power Sources* **175** 675–9

[13] Wang Y and Xia Y 2013 Recent progress in supercapacitors: from materials design to system construction *Adv. Mater.* **25** 5336–42

[14] Liu C *et al* 2010 Graphene-based supercapacitor with an ultrahigh energy density *Nano Lett.* **10** 4863–8

[15] Burke A 2007 R&D considerations for the performance and application of electrochemical capacitors *Electrochim. Acta* **53** 1083–91

[16] Pan H *et al* 2010 Carbon nanotubes for supercapacitor *Nanoscale Res. Lett.* **5** 654–68

[17] Xia J, Chen F, Li J and Tao N 2009 Measurement of the quantum capacitance of graphene *Nat. Nanotechnol.* **4** 505–9

[18] Wang Y *et al* 2011 Preventing graphene sheets from restacking for high-capacitance performance *J. Phys. Chem.* C **115** 23192–7

[19] Park S and Ruoff R S 2009 Chemical methods for the production of graphenes *Nat. Nanotechnol.* **4** 217–24

[20] Zhu Y *et al* 2010 Microwave assisted exfoliation and reduction of graphite oxide for ultracapacitors *Carbon* **48** 2118–22

[21] Schniepp H C *et al* 2006 Functionalized single graphene sheets derived from splitting graphite oxide *J. Phys. Chem.* B **110** 8535–9

[22] Jin M *et al* 2011 Facile physical route to highly crystalline graphene *Adv. Funct. Mater.* **21** 3496–501

[23] Stankovich S *et al* 2007 Synthesis of graphene-based nanosheets via chemical reduction of exfoliated graphite oxide *Carbon* **45** 1558–65

[24] Zhu Y *et al* 2011 Carbon-based supercapacitors produced by activation of graphene *Science* **332** 1537–41

[25] El-Kady M F *et al* 2012 Laser scribing of high-performance and flexible graphene-based electrochemical capacitors *Science* **335** 1326–30

[26] Yang H, Kannappan S, Pandian A S, Jang J, Lee Y S and Lu W 2015 Nanoporous graphene materials by low-temperature vacuum-assisted thermal process for electrochemical energy storage *J. Power Sources* **284** 146–53

[27] Li Y *et al* 2010 Catalytic performance of Pt nanoparticles on reduced graphene oxide for methanol electro-oxidation *Carbon* **48** 1124–30

[28] Acik M *et al* 2010 Unusual infrared-absorption mechanism in thermally reduced graphene oxide *Nat. Mater.* **9** 840–5

[29] Leofanti G *et al* 1998 Surface area and pore texture of catalysts *Catal. Today* **41** 207–19

[30] Yang M *et al* 2012 Mesoporous slit-structured NiO for high-performance pseudocapacitors *Phys. Chem. Chem. Phys.* **14** 11048–52

[31] Seri-Levy A and Avnir D 1993 The Brunauer–Emmett–Teller equation and the effects of lateral interactions. A simulation study *Langmuir* **9** 2523–9

[32] Prehal C *et al* 2017 Quantification of ion confinement and desolvation in nanoporous carbon supercapacitors with modelling and *in situ* x-ray scattering *Nat. Energy* **2** 16215

[33] Hantel M M, Weingarth D and Kötz R 2014 Parameters determining dimensional changes of porous carbons during capacitive charging *Carbon* **69** 275–86

[34] Rochester C C, Pruessner G and Kornyshev A A 2015 Statistical mechanics of 'unwanted electroactuation' in nanoporous supercapacitors *Electrochim. Acta* **174** 978–84

[35] Kowalczyk P *et al* 2005 Storage of hydrogen at 303 K in graphite slitlike pores from grand canonical Monte Carlo simulation *J. Phys. Chem.* B **109** 17174–83

[36] Zhao W *et al* 2011 Activated carbons with appropriate micropore size distribution for hydrogen adsorption *Int. J. Hydrog. Energy* **36** 5431–4

[37] Jagiello J *et al* 2013 2D-NLDFT adsorption models for carbon slit-shaped pores with surface energetical heterogeneity and geometrical corrugation *Carbon* **55** 70–80

[38] Jagiello J *et al* 2013 Carbon slit pore model incorporating surface energetical heterogeneity and geometrical corrugation *Adsorption* **19** 777–83

[39] Lawson C L and Hanson R J 1974 *Solving Least Squares Problems, Society for Industrial and Applied Mathematics* (Englewood Cliffs, NJ: Prentice-Hall) (https://doi.org/10.1137/1.9781611971217)

[40] Hansen C and O'Leary D P 1993 The use of the L-curve in the regularization of discrete III-posed problems *SIAM J. Sci. Comput.* **14** 1487–503

[41] Jiang D, Jin Z, Henderson D and Wu J 2012 Solvent effect on the pore-size dependence of an organic electrolyte supercapacitor *J. Phys. Chem. Lett.* **3** 1727–31

[42] Merlet C *et al* 2012 On the molecular origin of supercapacitance in nanoporous carbon electrodes *Nat. Mater.* **11** 306–10

[43] Shim Y and Kim H J 2010 Nanoporous carbon supercapacitors in an ionic liquid: a computer simulation study *ACS Nano* **4** 2345–55

[44] Jiang D, Jin Z and Wu J 2011 Oscillation of capacitance inside nanopores *Nano Lett.* **11** 5373–7

[45] Delhaes P 2001 *Graphite and Precursors* (Boca Raton, FL: CRC Press)

[46] Tuinstra F and Koenig J L 1970 Raman spectrum of graphite *J. Chem. Phys.* **53** 1126–30

[47] Ferrari A C and Robertson J 2000 Interpretation of Raman spectra of disordered and amorphous carbon *J. Phys. Rev.* B **61** 14095

[48] Kudin K N *et al* 2008 Raman spectra of graphite oxide and functionalized graphene sheets *Nano Lett.* **8** 36–41

[49] Lee G D *et al* 2005 Diffusion, coalescence, and reconstruction of vacancy defects in graphene layers *Phys. Rev. Lett.* **95** 205501

[50] Stone A J and Wales D J 1986 Theoretical studies of icosahedral C_{60} and some related species *Chem. Phys. Lett.* **128** 501–3

[51] Wang G *et al* 2008 Facile synthesis and characterization of graphene nanosheets *J. Phys. Chem.* C **112** 8192–5

[52] Yang D *et al* 2009 Chemical analysis of graphene oxide films after heat and chemical treatments by x-ray photoelectron and micro-Raman spectroscopy *Carbon* **47** 145–52
[53] Kozlowski C and Sherwood P M A 1984 X-ray photoelectron spectroscopic studies of carbon-fibre surfaces: IV. The effect of electrochemical treatment in nitric acid *J. Chem. Soc. Faraday Trans.* I **80** 2099–107
[54] Gao W *et al* 2009 New insights into the structure and reduction of graphite oxide *Nat. Chem.* **1** 403–8
[55] Wang G *et al* 2009 Graphene nanosheets for enhanced lithium storage in lithium ion batteries *Carbon* **47** 2049–53
[56] Conway B E 1999 *Electrochemical Supercapacitors: Scientific Fundamentals and Technological Applications* (New York, NY: Springer) (https://doi.org/10.1007/978-1-4757-3058-6)
[57] Zhang S *et al* 2006 Physical properties of ionic liquids: database and evaluation *J. Phys. Chem. Ref. Data* **35** 1475–517
[58] Bisquert J *et al* 1998 Impedance of constant phase element (CPE)-blocked diffusion in film electrodes *J. Electroanal. Chem.* **452** 229–34
[59] Hao G-P *et al* 2016 Design of hierarchically porous carbons with interlinked hydrophilic and hydrophobic surface and their capacitive behavior *Chem. Mater.* **28** 8715–25
[60] Zhang S and Pan N 2015 Supercapacitors performance evaluation *Adv. Energy Mater.* **5** 1401401
[61] Brown C J 1954 The crystal structure of ethylene carbonate *Acta Crystallogr.* **7** 92–6
[62] Liu S *et al* 2010 Influence of imidazolium-based ionic liquids on the performance of ionic polymer conductor network composite actuators *Polym. Int.* **59** 321–8
[63] Aken K L V *et al* 2014 Effect of cation on diffusion coefficient of ionic liquids at onion-like carbon electrodes *J. Phys.: Condens. Matter* **26** 284104
[64] Lockett V, Sedev R and Ralston J 2008 Differential capacitance of the electrical double layer in imidazolium-based ionic liquids: influence of potential, cation size, and temperature *J. Phys. Chem.* C **112** 7486–95
[65] Iklyumbur T J *et al* 2017 Dielectric properties of 1-ethyl-3-methyl-imidazolium tetrafluoroborate (EMIM-BF4) using Cole–Cole relaxation model *Phys. Sci. Int. J.* **13** 1–6
[66] Yang X *et al* 2013 Liquid-mediated dense integration of graphene materials for compact capacitive energy storage *Science* **341** 534–7